UNIVERSITY OF COPENHAGEN

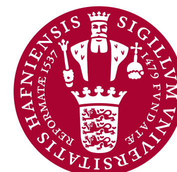
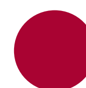

Correlation between Electrical Transport and Nanoscale Strain in InAs/In06Ga04As Core-Shell Nanowires

Zeng, Lunjie; Gammer, Christoph; Ozdol, Burak; Nordqvist, Thomas; Nygard, Jesper; Krogstrup, Peter; Minor, Andrew M.; Jaeger, Wolfgang; Olsson, Eva

Published in:
Nano Letters

DOI:
10.1021/acs.nanolett.8b01782

Publication date:
2018

Document version
Publisher's PDF, also known as Version of record

Document license:
CC BY-NC

Citation for published version (APA):
Zeng, L., Gammer, C., Ozdol, B., Nordqvist, T., Nygard, J., Krogstrup, P., ... Olsson, E. (2018). Correlation between Electrical Transport and Nanoscale Strain in InAs/$In_{06}Ga_{04}$As Core-Shell Nanowires. *Nano Letters*, *18*(8), 4949-4956. https://doi.org/10.1021/acs.nanolett.8b01782

Download date: 09. Apr. 2020

This is an open access article published under an ACS AuthorChoice License, which permits copying and redistribution of the article or any adaptations for non-commercial purposes.

ACS AuthorChoice

NANO LETTERS

Letter

Cite This: Nano Lett. 2018, 18, 4949−4956

pubs.acs.org/NanoLett

Correlation between Electrical Transport and Nanoscale Strain in InAs/$In_{0.6}Ga_{0.4}As$ Core−Shell Nanowires

Lunjie Zeng,[†] Christoph Gammer,[‡] Burak Ozdol,[§] Thomas Nordqvist,[∥] Jesper Nygård,[∥] Peter Krogstrup,[∥] Andrew M. Minor,[§,⊥] Wolfgang Jäger,[†,#] and Eva Olsson*,[†]

[†]Department of Physics, Chalmers University of Technology, 41296 Gothenburg, Sweden

[‡]Erich Schmid Institute of Materials Science, Austrian Academy of Sciences, 8700 Leoben, Austria

[§]National Center for Electron Microscopy, Molecular Foundry, Lawrence Berkeley National Laboratory, Berkeley, California 94720, United States

[∥]Niels Bohr Institute, University of Copenhagen, 2100 Copenhagen, Denmark

[⊥]Department of Materials Science and Engineering, University of California, Berkeley, California 94720, United States

[#]Institute of Materials Science, Christian-Albrechts-University Kiel, 24118 Kiel, Germany

Supporting Information

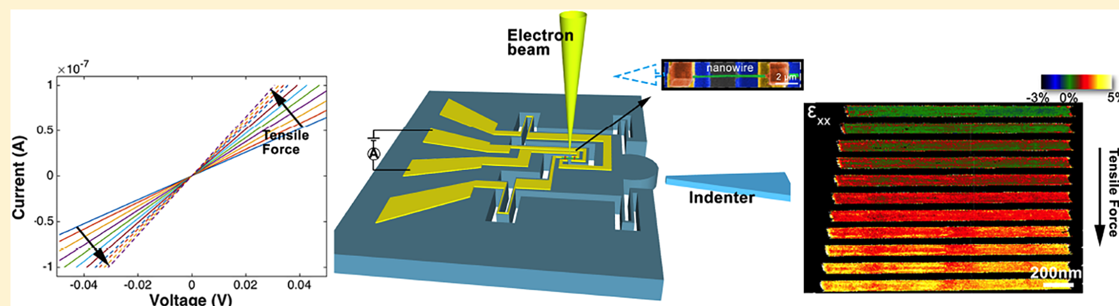

ABSTRACT: Free-standing semiconductor nanowires constitute an ideal material system for the direct manipulation of electrical and optical properties by strain engineering. In this study, we present a direct quantitative correlation between electrical conductivity and nanoscale lattice strain of individual InAs nanowires passivated with a thin epitaxial $In_{0.6}Ga_{0.4}As$ shell. With an in situ electron microscopy electromechanical testing technique, we show that the piezoresistive response of the nanowires is greatly enhanced compared to bulk InAs, and that uniaxial elastic strain leads to increased conductivity, which can be explained by a strain-induced reduction in the band gap. In addition, we observe inhomogeneity in strain distribution, which could have a reverse effect on the conductivity by increasing the scattering of charge carriers. These results provide a direct correlation of nanoscale mechanical strain and electrical transport properties in free-standing nanostructures.

KEYWORDS: *InAs nanowire, strain mapping, piezoresistance, transmission electron microscopy*

Nanoscale III−V semiconductor materials are essential components in electronic and optical devices such as high-speed transistors, photovoltaics, and photodetectors.[1−9] In contrast to bulk materials, nanocrystals (such as nanowires) offer new possibilities for strain engineering by the growth of heteroepitaxial layers or by mechanical manipulation. The quasi-1D geometry combined with the high crystal quality of the nanowires often enables the nanowires to withstand more mechanical strain compared with their bulk counterparts. Significant electromechanical responses have been found in various semiconductor nanowires, although the origin of the profound electromechanical effects is still under debate.[10−18] Among the semiconductor nanowires studied, InAs nanowires possess some unique properties such as strong spin−orbital coupling, a relatively narrow band gap, and a high electron mobility.[7,9,19−21] Previously, considerable piezoresistive and piezoelectric effects in InAs nanowires have been reported.[11,22] Surface effects, such as surface-charge accumulation and ionized surface states, have been found to strongly affect the electrical and photonic properties as well as the electromechanical properties of bare InAs nanowires.[23−25] The change in the density of accumulated surface charge with strain was considered the main reason for the strong electromechanical response of bare InAs nanowires.[11] Nonetheless, electromechanical characteristics of InAs nanowires with suppressed surface effects have not yet been studied. Especially, studies of the correlation between mechanical properties and the electrical transport properties of single InAs nanowires with reduced surface effects are still lacking.

Received: May 2, 2018
Revised: July 15, 2018
Published: July 25, 2018

Downloaded via COPENHAGEN UNIV LIBRARY on December 6, 2018 at 14:13:23 (UTC).
See https://pubs.acs.org/sharingguidelines for options on how to legitimately share published articles.

ACS Publications © 2018 American Chemical Society

In this paper, we have carried out such studies and show that there is a direct correlation between electrical transport and the nanoscale lattice strain of single crystalline InAs nanowires. The InAs nanowires were passivated with a thin coherently strained $In_{0.6}Ga_{0.4}As$ radial shell to reduce surface effects. Electrical conductivity and nanoscale mechanical strain measurements of the nanowires were performed simultaneously with an electromechanical in situ transmission electron microscopy (TEM) set up. In situ straining, mechanical measurement, and electrical characterization were enabled by an in situ TEM holder. Quantitative nanoscale strain analysis on the nanowire was carried out using scanning TEM (STEM) combined with nanobeam electron diffraction (NBED). By straining the crystal lattice, the charge carrier transport is altered by modifications in the band structure and charge carrier scattering characteristics engendering an intriguing insight into the electromechanical behavior of InAs nanowires.

The surface of the InAs nanowires used in this study is passivated with a thin $In_{0.6}Ga_{0.4}As$ shell, as presented in Figure 1a,b. The nanowire morphology appears uniform. The nanowire has a diameter of about 84 nm and is approximately 10 μm long. The nanowires show single crystalline wurtzite structure in both the core and the shell (Figure 1). Radial growth of a larger band gap material (~0.68 eV for bulk $In_{0.6}Ga_{0.4}As$) compared to the core (~0.35 eV for bulk InAs) is used here as an effective method to reduce surface charge accumulation and ionized states for InAs nanowires.[26,27] In general, a considerable lattice mismatch between the core and shell materials may result in inhomogeneities at the interface, such as misfit dislocations or change of crystal structure, which will increase charge carrier scattering and reduce the charge carrier mobility. The nominal lattice mismatch between bulk wurtzite InAs and $In_{0.6}Ga_{0.4}As$ is about 2.7% (see Supporting Information S1). Here, we have a core−shell nanowire structure, which will affect the distributions and magnitudes of lattice strain in the InAs core (diameter ~80 nm) and in the $In_{0.6}Ga_{0.4}As$ shell (~4 nm). A detailed strain analysis near the core−shell interface of the nanowire is shown in Figure S4. A thorough inspection revealed no dislocations along the nanowire length (see Figures 1 and S2). Selected area electron diffraction (SAED) analysis also confirmed the absence of stacking faults and dislocations (Supporting Information S3).

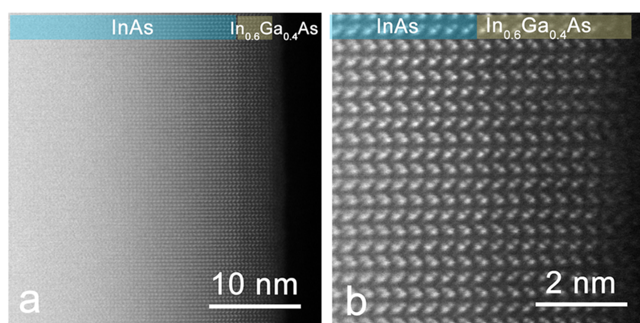

Figure 1. STEM annular dark field (ADF) images of an InAs/$In_{0.6}Ga_{0.4}As$ core−shell nanowire. (a) Overview micrograph showing the contrast difference between the InAs core and $In_{0.6}Ga_{0.4}As$ shell. (b) A magnified image of the interface between the core and the shell. Both the core and the shell have wurtzite structure. The interface is coherent without dislocations despite the lattice mismatch between the core and the shell.

The core and shell appear to be coherently strained, with the shell fully passivating the InAs core surface.

To investigate the correlation between mechanical strain and the electrical transport properties of such surface-passivated InAs nanowires, a Hysitron PI95 nanoindenter holder with an electrical push-to-pull (EPTP) microelectromechanical system (MEMS) device was used for the in situ TEM studies; see the Methods section and Supporting Information for a more detailed description. The nanowires were placed across the gap between a movable and a fixed part in the EPTP device and connected to an electrical circuit (see Figure 2a). Tensile stress was applied on the nanowires by a nanoindenter through the push-to-pull mechanism. Direct and quantitative measurements of the stress, strain, and electrical conductivity of single nanowires were performed simultaneously, while the nanowires were pulled in tension using the EPTP device.

The tensile stress applied on the nanowire was determined from the in situ TEM measurements as described in the following. The force applied to the nanowire (Figure 2c) was determined by the difference in load applied to the MEMS device with and without the nanowire (Figure 2b). The force−displacement curves before and after the fracture of the nanowire are both linear, indicating the elastic deformation of the EPTP device and the nanowire as well as a brittle fracture of the InAs nanowire. The nanowire fractured when the total load applied on the EPTP MEMS device was around 110 μN. A combination of scanning electron microscopy (SEM) and TEM was used to determine the original diameter and length (between the two electrical contacts) as well as the changes in dimensions of the nanowire as a function of the applied load. As a result, the stress applied on the nanowire was determined based on the force and geometry measurements.

The in situ quantitative measurements of lattice strain and nanoscale strain distribution were carried out by STEM−NBED strain mapping. STEM−NBED has been demonstrated to be a reliable method for measuring mechanical strain in crystalline materials with high spatial resolution, a large field of view, and high precision.[28,29] The electron beam diameter was about 2 nm with a convergence angle of ~2 mrad. The electron beam was scanned over an area of 2 μm × 140 nm with a step size of about 4 nm, and a NBED pattern was acquired at each beam position. The NBED patterns were acquired with the electron beam aligned along the [1−100] zone axis of InAs (Supporting Information S8). At each beam position, axial and radial strain in the nanowire was determined by measuring the displacements of the (0002) and (11−20) diffraction spots in the NBED pattern relative to those when no strain was applied on the nanowire. By measuring lattice strain at every beam position, the spatial strain distribution in the nanowire was obtained and presented as strain map for the different stress loads applied (Figure 3a,b). In situ STEM−NBED measurements were performed while the nanowire was under stress. Strain maps corresponding to different tensile stresses applied on the nanowire were then calculated. The detailed spatial strain distributions along the (0002) (defined as the x axis) and the (11−20) directions (y axis) were obtained and plotted as ε_{xx} and ε_{yy}, respectively (Figure 3a,b). The rotation of the crystal lattices was also measured based on the intensity distribution in the diffraction patterns of the NBED maps. In general, the lattice structure of the InAs nanowires in this study shows very little rotation (less than 1°), even at the highest stress level (Figure 3c).

DOI: 10.1021/acs.nanolett.8b01782
Nano Lett. 2018, 18, 4949−4956

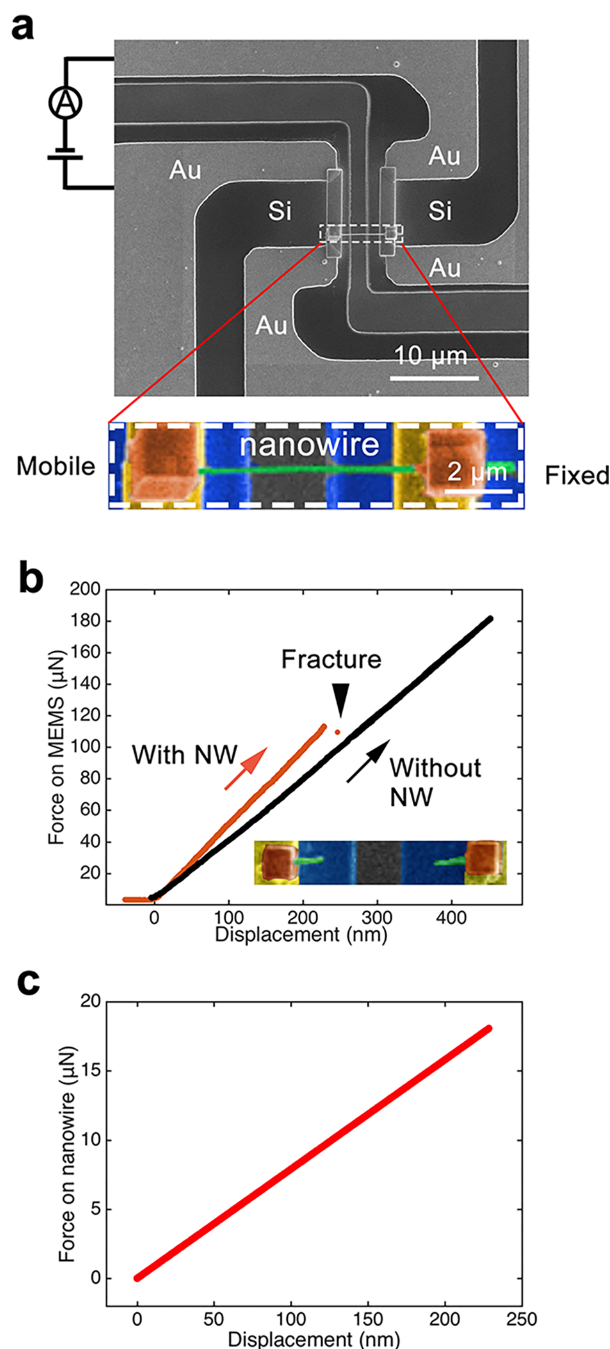

Figure 2. EPTP MEMS device and mechanical measurement on single core-shell InAs nanowire in the in situ TEM instrument. (a) Top: an SEM image of the EPTP device with an core-shell InAs nanowire mounted across the gap between the mobile and fixed parts of the device. The EPTP device is made of Si with four Au electrodes deposited on it. A schematic of the electrical circuit is also shown. Bottom: a magnified image of the area marked by the dashed window in the upper image. The ion beam induced deposition (IBID) of Pt (yellow) on the EPTP device (blue) was used to connect the Au electrodes and establish electrical contact. The nanowire (green) is fixed on the IBID Pt stripes by electron beam induced deposition (EBID) of Pt (orange). The gray part is the gap between the fixed and mobile parts and allows for the TEM investigation of the nanowire during in situ TEM measurements. (b) Force−displacement curves of the EPTP MEMS device obtained before (brown) and after (black) the fracture of the nanowire. The inset shows a SEM image of the fractured nanowire. (c) Force−displacement curve of the nanowire deduced from panel b.

The axial ε_{xx} maps provide detailed and quantitative information about the spatial distribution of strain along the axial direction of the nanowire and also the evolution of the axial strain resulting from external tensile stresses (Figure 3a). When there is no stress applied, the mean tensile strain in the nanowire core is around zero, although in some small areas, there is either tensile or compressive strain (the first strain map from the top in Figure 3a). This local strain in the nanowire without any externally applied stress is likely due to the nanowire transfer process when a small amount of stress may be introduced in the nanowire during the mechanical fixing of the nanowire onto the EPTP device. As the applied load from the nanoindenter increases, strain distribution within the nanowire evolves gradually. As shown by the axial strain maps (ε_{xx}; Figure 3a), the tensile strain seems to initially emerge in localized areas close to the surfaces of the nanowire. Subsequently, more and more areas within the nanowire show tensile strain as the applied stress increases, while the rest of the nanowire area is still not strained. When the force applied on the nanowire reaches ~7.79 μN, the entire nanowire seems to be homogeneously strained, as observed from the even contrast in the ε_{xx} map. When the force applied on the nanowire is larger than 9.43 μN, a region of the nanowire close to the center always shows lower tensile strain compared to rest of the nanowire. The ε_{xx} maps show spatial radial and axial inhomogeneity in strain distribution (Figure 3a). Moreover, the average strain value ($\langle\varepsilon_{xx}\rangle$) over the whole strain map is calculated. The average strain $\langle\varepsilon_{xx}\rangle$ increases with force, reaching values of 0.187%, 0.466%, and 0.837% at 1.19, 2.84, and 4.49 μN, respectively. When the nanowire experiences a tensile strain along the axial direction, the lattice in the nanowire is expected to be elastically compressed in the radial direction due to the positive Poisson's ratio of these materials.[30] The spatial distribution of the compressive strains within the nanowire (ε_{yy}) under different stresses also shows complex behaviors. As the applied stress increases, compressive strain emerges initially in some localized areas in the nanowire (Figure 3b). Thereafter, more and more regions in the nanowire show compressive lattice strain though there are always areas in the nanowire in which the lattice is not strained. From these quantitative spatial strain distribution maps, the corresponding probability histograms are calculated and displayed in Figure 3d. The lattice strain along both the x and y directions are inhomogeneous within the nanowire under tensile stress, whereas the average strain values $\langle\varepsilon_{xx}\rangle$ gradually increase and the average strain values $\langle\varepsilon_{yy}\rangle$ gradually decrease with applied stress. The spread of measured strain values in each strain map usually varies around 1%. The origin of this spread in strain values is unclear but may be related to the inherent lattice strain existing in the nanowire due to the core−shell structure. Surface roughness at the nanometer scale may also contribute to the observed strain distributions. Further studies are needed to fully understand the cause for the strain inhomogeneity at the nanometer scale in the nanowire.

Nonetheless, strain analyses based on STEM−NBED maps allow a direct quantification of the elastic strain within the nanowire. The average strain values $\langle\varepsilon_{xx}\rangle$ and $\langle\varepsilon_{yy}\rangle$ were calculated from the strain maps and considered as the elastic strain of the whole nanowire. In such a way, we directly determined the elastic strain within the nanowire. The Poisson's ratio of the InAs/$In_{0.6}Ga_{0.4}As$ core−shell nanowire was also calculated, based on the $\langle\varepsilon_{xx}\rangle$ and $\langle\varepsilon_{yy}\rangle$ values, to be ~0.36. Moreover, strain mapping also clearly and quantita-

DOI: 10.1021/acs.nanolett.8b01782
Nano Lett. 2018, 18, 4949−4956

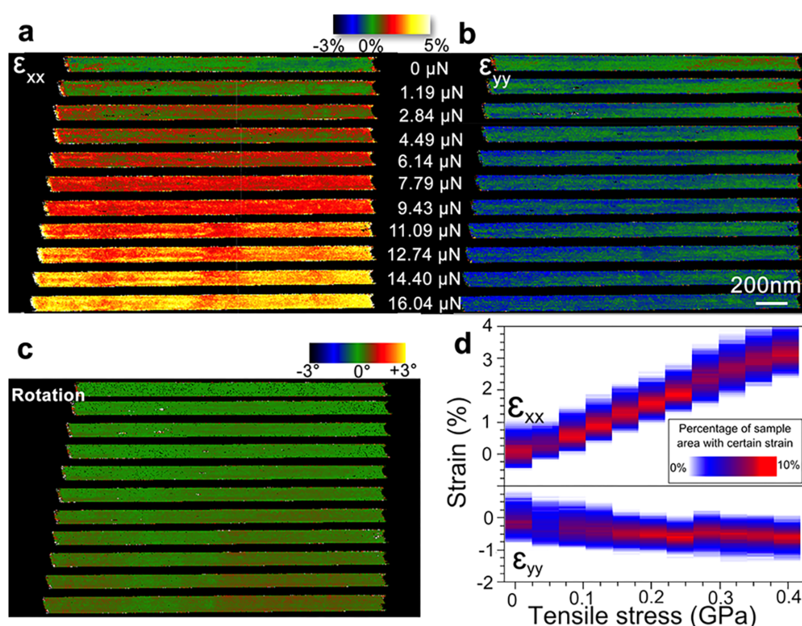

Figure 3. Lattice strain distribution within the core-shell InAs nanowire under tensile stresses unveiled by STEM−NBED measurements. (a) Lattice strain distribution along the nanowire length direction with different tensile forces applied on the nanowire. (b) The corresponding strain distribution maps of the nanowire for strain along the direction perpendicular to the nanowire length direction. (c) The corresponding rotation angle maps of the nanowire. (d) Quantitative strain distribution histograms at different stress levels in the nanowire. The *X* axis shows stress applied on the nanowire. The *Y* axis is the lattice strain. The colors indicate the probability of certain strain existing in the strain maps, with red showing higher probabilities than blue.

tively shows the spatial fluctuations of lattice deformation within the nanowire at the nanometer scale for different stress levels. Interestingly, despite those inhomogeneous strain distributions, the nanowire as a whole seems to deform elastically under tensile stress before fracture, as indicated by the linear characteristics of force−displacement curve (Figure 2b,c). Our strain analyses also unravel the evolution of lattice strain within the nanowire, containing rich information about the creation and development of lattice strain in such a nanosized crystal under external mechanical stimuli.

To correlate electrical transport properties with the stress and the strain characteristics, simultaneous transport measurements were conducted during the in situ TEM experiments. All current−voltage ($I-V$) characteristics measured for nanowires with electrical contacts at both ends show a linear behavior, thus confirming Ohmic contact behavior (Figure 4a). $I-V$ measurements were also performed for larger voltage range than that shown in Figure 4a (Supporting Information S9). The $I-V$ characteristics at a larger voltage range show the same linear behavior as those in smaller voltage range. To avoid the overheating of the nanowire, the effect of stress on the $I-V$ characteristics was measured within the relatively small applied voltage range, as shown in Figure 4a. It should also be noted that the contacts between the nanowire and the EPTP device remain mechanically stable based on the reproducible STEM, load−displacement, and $I-V$ measurements (see Supporting Information S10). Figure 4b shows STEM micrographs of a nanowire under different tensile stresses. Piezoelectric effects in InAs nanowires have previously been reported and shown to result in asymmetric $I-V$ characteristics.[22] In contrast, our $I-V$ curves are linear and symmetric, suggesting a minimal piezoelectric effect on the $I-V$ measurements of the individual InAs nanowires. The slope of the $I-V$ curves, i.e., the resistance of the nanowire, changes continuously with tensile stress (Figure 5a). At the maximum

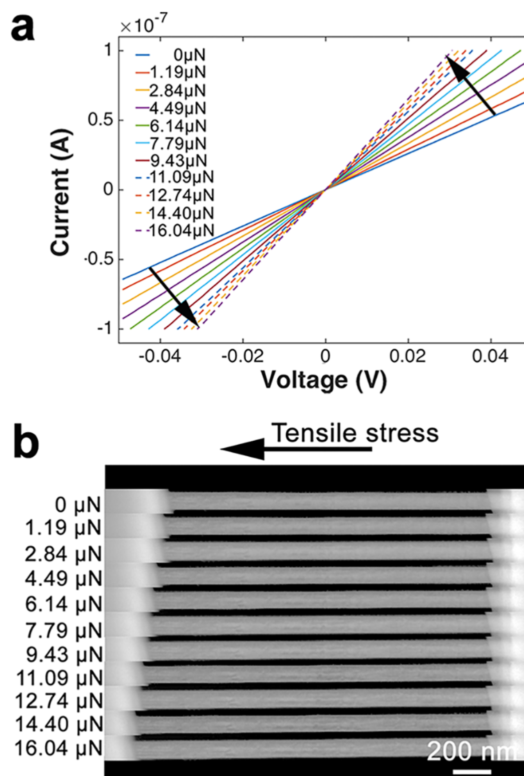

Figure 4. Effect of tensile stress on the electrical transport properties of the core-shell InAs nanowire. (a) Current−voltage characteristics of the nanowire when different forces were applied on the nanowire. Arrows indicate the direction of the increase of force. (b) The corresponding STEM ADF images of the nanowire under the absence of stress and for different tensile stresses.

DOI: 10.1021/acs.nanolett.8b01782
Nano Lett. 2018, 18, 4949−4956

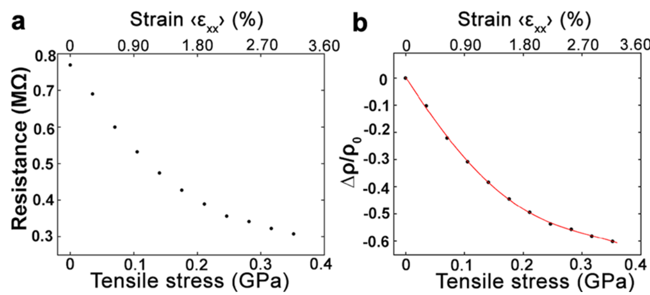

Figure 5. Electromechanical properties of the core-shell InAs nanowire: (a) Resistance as a function of tensile stress and average tensile strain $\langle \varepsilon_{xx} \rangle$. (b) The relative change in resistivity of the nanowire as a function of tensile stress and average tensile strain $\langle \varepsilon_{xx} \rangle$. Red curve shows a polynomial fitting to the experimental data for extracting the piezoresistance coefficients of the nanowire.

tensile strain before fracture ($\langle \varepsilon_{xx} \rangle \approx 3.2\%$), the resistance of the core-shell InAs nanowire has decreased by more than 60% compared to the resistance without any applied stress (Figure 5a). The change in resistance with mechanical strain can be characterized by a gauge factor (GF), which is defined as the ratio between the change in resistance and the average strain:

$$\mathrm{GF} = \frac{\frac{\Delta R}{R_0}}{\varepsilon} = \frac{\frac{\Delta R}{R_0}}{\langle \varepsilon_{xx} \rangle}$$

where ΔR is the change in resistance and R_0 is the resistance at zero stress. The GF value of the InAs nanowire varies nonlinearly as a function of strain and decreases gradually with strain. The measured GF values vary from ~46.7 at small strains to ~8.4 at around the maximum tensile strain level. The change in resistance of the nanowire is likely to originate from the change in geometry (length and diameter) and from the change in resistivity as a result of the mechanical strain. Therefore, the gauge factor can be expressed as:

$$\mathrm{GF} = \frac{\frac{\Delta R}{R}}{\langle \varepsilon_{xx} \rangle} = \frac{\frac{\Delta \rho}{\rho_0}}{\langle \varepsilon_{xx} \rangle} + 1 + 2\nu$$

where ρ_0 is the resistivity of the nanowire under zero stress, $\Delta\rho$ is the change in resistivity, and ν is the Poisson's ratio of the nanowire. The observed decrease in electrical resistance of our InAs nanowires is in contradiction to the expected increase in resistance when only changes in nanowire dimensions are considered. From this result, we can conclude that the change in resistance is due to the effect of strain on the resistivity.

The relative change in resistivity of the nanowire as a function of the tensile stress and strain is shown in Figure 5b. The resistivity of the nanowire at zero stress is found to be about $5.5 \times 10^{-3} \Omega\cdot\mathrm{m}$, which is comparable with values previously reported for InAs and InAsP nanowires.[12,31] At the highest tensile stress before fracture, the resistivity of the nanowire has dropped by approximately 60% in comparison to that at zero stress. The quantitative variation in resistivity due to applied stress is commonly described by the piezoresistance effect. As the applied electric field is aligned with the uniaxial stress and the measured current, the longitudinal piezoresistance coefficient, π^l, can be defined and measured as the relative change in resistivity per unit stress:

$$\pi^l = \frac{1}{\sigma}\frac{\Delta\rho}{\rho_0}$$

where ρ_0 is the resistivity of the nanowire under zero stress, σ is the stress applied on the nanowire, and $\Delta\rho$ is the change in resistivity.

The InAs/$In_{0.6}Ga_{0.4}As$ nanowire shows a nonlinear piezoresistive response. Figure 5b clearly shows the nonlinear piezoresistance characteristics of the $\Delta\rho/\rho_0$ curve, which is different from the electromechanical behavior of bare InAs nanowire without the shell (Supporting Information S12). The nonlinearity in piezoresistance effect is believed to be a result of the nonparabolic shape of the energy bands in nanowires.[10−12] Due to the obvious nonlinearity in piezoresistance, the piezoresistance effect in the core−shell InAs nanowire can be described as:[32]

$$\frac{\Delta\rho}{\rho} = \pi_1^l\sigma + \pi_2^l\sigma^2 + \pi_3^l\sigma^3 + \cdots$$

where π_i^l is the i-th longitudinal piezoresistance coefficient. By fitting the nonlinear piezoresistance effect to the $\Delta\rho/\rho_0 - \sigma$ data with a fourth-order polynomial, the piezoresistance coefficients of the InAs/$In_{0.6}Ga_{0.4}As$ nanowire from first- to fourth-order are found to be $\pi_1^l = -3.4 \times 10^{-9}\ \mathrm{Pa}^{-1}$, $\pi_2^l = 1.9 \times 10^{-18}\ \mathrm{Pa}^{-1}$, $\pi_3^l = 19.3 \times 10^{-27}\ \mathrm{Pa}^{-1}$, and $\pi_4^l = -33.5 \times 10^{-36}\ \mathrm{Pa}^{-1}$; see the red curve in Figure 5b.

The first-order piezoresistance coefficient of the InAs/$In_{0.6}Ga_{0.4}As$ core−shell InAs nanowire is compared to the piezoresistance coefficient obtained in bulk and other semiconductor nanowires. We found that π_1^l of the core−shell InAs nanowire used in this study is 2 orders of magnitude larger than that of InAs bulk material, which has a piezoresistance coefficient of $\sim -5 \times 10^{-11}\ \mathrm{Pa}^{-1}$.[33] It is also about an order of magnitude larger than the first-order piezoresistance coefficient of InAsP and InAs nanowires reported previously.[12,22]

It is worth noting that the resistance obtained from our in situ $I-V$ measurements consists of contributions from the nanowire itself and the contact resistance at the two electrical contacts between the nanowire and the EPTP device. The contact resistance is insignificant compared to the resistance of the nanowire due to two reasons. First, it is known that InAs easily forms Ohmic contacts with various metals because of its small band gap and Fermi-level pinning at the surface.[34] As a result, the Schottky barrier and contact resistance at the contacts between the nanowire and EPTP device are expected to be small. This is evident in the linear $I-V$ characteristics of the nanowire used in our study. Second, the resistance value at zero stress in our measurement is comparable with previously reported four-probe measurements on InAs nanowires.[31] It also indicates that the contact resistance is not dominating in our measurements. Moreover, according to our repeated $I-V$ measurements, TEM imaging, and strain measurements, the contacts between the nanowire and the EPTP device are stable under applied mechanical stresses. Thus, the strain induced resistance changes are not likely due to the changes in contact conditions. The resistance changes we observed come from the nanowire.

There are several effects that the $In_{0.6}Ga_{0.4}As$ shell may have on the charge transport in InAs nanowire. The shell has a larger band gap than the InAs core. It has been shown previously that such a shell will largely reduce surface band bending and charge accumulation.[26,35] Thus, the charge carriers will populate the core instead of the InAs nanowire surface as in bare InAs nanowire. In addition, InAs has a larger electron mobility compared to $In_{0.6}Ga_{0.4}As$,[3] resulting in preferred charge transport in the InAs core in the core−shell

DOI: 10.1021/acs.nanolett.8b01782
Nano Lett. 2018, 18, 4949−4956

nanowire. Therefore, the piezoresistance effect we observed of the core−shell nanowire is likely mainly from the contribution of the InAs core. As a result, the observed resistance variation in InAs/$In_{0.6}Ga_{0.4}As$ nanowire is from the change in resistivity of InAs nanowire core induced by mechanical strain. It is in contrast to the electromechanical behavior of bare InAs nanowire, where the piezoresistive effect was believed to be from the change in surface charge density induced by uniaxial strain.[11] The passivation effect of the $In_{0.6}Ga_{0.4}As$ shell thus changes the electromechanical properties of the InAs nanowire, as observed in our study.

Strain effects on resistivity of nanowires can be qualitatively understood by Drude's model. From this model, the resistivity change is caused by the carrier density (n) change, mass (m^*) shift, and scattering-rate (or scattering time τ) variation induced by strain. They can normally all be attributed to strain altered band structures.[36] Strain can cause band-edge shift and band splitting of both the conduction and the valence bands (Supporting Information S13). With uniaxial tensile strain along the length direction, the lowest conduction band of InAs nanowire will shift down along energy axis. For the top valence band, the originally degenerated heavy-hole (HH) and light-hole (LH) bands at the Γ point will split. The HH band will move up in energy, while the LH band will shift down in energy. The band gap of InAs is then defined by the difference in energy between the bottom of conduction band and the top of HH band at Γ point. In addition, the shift in Fermi level due to strain is insignificant. Such shift and splitting of the energy bands due to uniaxial tensile strain result in a reduction in the band gap of InAs nanowire, which can induce significant change of intrinsic carrier density. For undoped semiconductors, the carrier concentration can be affected by lattice strain via the change in the band gap of the semiconductors, and consequently:

$$n = \sqrt{N_c N_v}\, e^{-E_g/2kT}$$

where N_c and N_v are effective density of states in conduction and valence band, respectively, E_g is energy band gap of the InAs nanowire, k is the Boltzmann constant, and T is the temperature of the material. At room temperature, N_c and N_v is about 8.7×10^{16} cm^{-3} and 6.6×10^{18} cm^{-3} for InAs, respectively.[37] Significant changes in band gap values as a result of lattice strain in various semiconductor nanowires have been reported before.[38−40] Tensile strain can result in a reduction of the band gap of InAs.[11,41] According to tight-binding simulations (Supporting Information S13), the band gap of InAs can decrease by ∼0.15 eV under 3% tensile strain along the [0001] direction. Such a change in band gap will give rise to around an order of magnitude increase in conduction electron density in InAs nanowire, which is consistent with the finding reported before.[11] The change in conduction electron density alone will contribute to an order of magnitude decrease in the resistivity of the InAs nanowire. In the InAs/$In_{0.6}Ga_{0.4}As$ core−shell nanowire, the resistivity of the nanowire drops about 60% at maximum tensile stress. The corresponding uniaxial tensile strain is about 3% (Figure 5b). This means that instead of an expected decrease of more than 90% in resistivity, we observe a significantly smaller decrease. The discrepancy is presumably due to a strain effects on carrier transport. This counteracts an increase in charge carrier concentration due to band gap narrowing.

Strain can also affect carrier transport through strain induced band structure variation. Strain can cause a band-warping effect, which can be understood by symmetry considerations.[42] Energy bands follow the symmetry of the Brillouin zone, which is determined by the macroscopic crystal symmetry. Uniaxial mechanical stress reduces the crystal symmetry, so the shape of the energy bands change accordingly, causing band warping. Under effective mass approximation, band warping will change the carrier masses at both the conduction-band minimum and the valence-band maximum in InAs. In addition, the aforementioned band splitting in valence band will also change carrier mass due to the separation of HH and LH bands. However, the change in effective carrier mass in III−V semiconductors due to strain-induced band splitting and warping is not significant and usually smaller than 5%.[43,44] Moreover, among the scattering mechanisms that affect the scattering rate of charge carriers, phonon scattering is normally considered to be dominating in semiconductors at room temperature. However, because the conduction band of InAs is singly degenerated, the scattering rate of conduction electrons in InAs is not affected significantly by strain.

Uniaxial tensile stress results in the strong inhomogeneity of lattice strain distribution in the core−shell InAs nanowire, as observed in the STEM−NBED measurements (Figure 3). As discussed above, such fluctuations in strain distribution can also affect charge transport and mobility in the nanowire. The local variation in strain can result in changes in the electronic band structure, which will induce local changes in the carrier concentration and the effective mass of the conduction electrons. In particular, the spatial variation in band gap at the nanometer scale within the nanowire will cause energy barriers for the transport of conduction electrons. Those barriers will increase the electron scattering and consequently decrease the mobility of the charge carriers. The distribution of the energy barriers is directly related to the extent of spatial inhomogeneity of strain. Strong strain inhomogeneity can give rise to confined channels for transport of charge carriers. The spatially confined charge transport will also increase the resistivity of the whole nanowire, which reduces the effect of carrier concentration change on the piezoresistance effect of the nanowire.

In summary, we have studied the intrinsic mechanical and electromechanical properties of individual InAs nanowires. Mechanical stress, lattice strain, and electrical transport characteristics of an InAs/$In_{0.6}Ga_{0.4}As$ core−shell nanowire were measured simultaneously using an electromechanical in situ TEM set up. In particular, the elastic lattice strain in the nanowire was directly and quantitatively determined by STEM−NBED mapping with nanometer resolution, while mechanical stress and electrical transport properties were measured simultaneously. The resistivity of the nanowires shows a sensitive response to external tensile stress. The electromechanical properties of the core−shell nanowire differ from the bare InAs nanowire. The piezoresistance coefficient of the core−shell nanowire was found to be about 2 orders of magnitude larger than bulk InAs and also larger than the bare InAs nanowire. Furthermore, the change in resistivity in the core−shell nanowire can be largely attributed to a reduction in band gap that increases the conduction electron concentration in InAs. We also observed a nanoscale inhomogeneity in the strain distributions of the core−shell nanowire using STEM−NBED strain mapping. While an increasing overall strain increases carrier concentration, local inhomogeneity in strain

DOI: 10.1021/acs.nanolett.8b01782
Nano Lett. 2018, 18, 4949−4956

distribution can have a reversed effect through the introduction of local scattering sites. Our study shows the unique mechanical and electromechanical properties of surface passivated InAs nanowires. The properties may be utilized in applications such as ultrasensitive nanoscale sensors.

Methods. *Nanowire Growth.* The core−shell nanowires used in this study are grown in a molecular beam epitaxy system on InAs(111)B substrates in a two-step process. First approximately 10 μm long Au catalyzed InAs nanowires are grown along the ⟨0001⟩ direction via the vapor−liquid−solid method at a substrate temperature T_{sub} = 420 °C with an In flux corresponding to a planar growth rate of 0.5 μm/h and an effective As_2-to-In flux ratio of 20. These growth conditions yield a pure wurtzite (WZ) crystal structure with no observed stacking faults. Subsequently, a shell of InGaAs is grown with a T_{sub} = 360 °C and a Ga flux corresponding to a planar growth rate of 0.33 μm/h, keeping As_2 flux constant.

Nanowire Transfer. For the in situ TEM studies, individual nanowires were lifted out and mounted on EPTP device in an FEI Strata focus ion beam − scanning electron microscope (FIB-SEM) instrument. The nanowires were put across the gap with a width of about 2.5 μm between a movable and a fixed part of the EPTP device. This gap allows for the TEM investigation of the nanowires. The nanowire was connected to the electrical contacts on the EPTP device with electron beam induced deposition (EBID) and ion beam induced deposition (IBID) of Pt in FIB-SEM (Supporting Information S5 and S6).

TEM. High-resolution STEM imaging was carried out using the TEAM 0.5 microscope operated at 300 kV.[45] ADF STEM images were acquired with a beam convergence angle of ∼17 mrad and semicollection angles of 50−270 mrad. The TEM specimens used for STEM imaging were prepared by mechanically removing InAs nanowires from the growth substrate and subsequently dispersing them on an amorphous carbon support film resting on a Cu TEM grid. The in situ TEM experiments were performed using the TEAM 1 microscope operated at 300 kV.[46] A Gatan K2 direct electron detector camera attached to the TEAM 1 microscope was used to record the NBED maps. In the STEM−NBED measurements performed in this study, the electron beam was focused to around 2 nm in diameter with a convergent angle of ∼2 mrad. The electron beam was scanned over an area with the size of 2 μm × 140 nm with a step size of about 4 nm. At each beam position, a NBED pattern was acquired with an exposure time of 2.5 ms with the K2 camera. Each diffraction pattern was obtained with the full frame of the camera, giving rise to 1920 × 1792 pixels in each diffraction pattern. The lattice distances and, hence, the lattice strain were measured directly and accurately based on the distances between the Bragg spots in NBED patterns. The in situ tensile test and electrical transport properties measurement were performed using a Hysitron PI95 nanoindenter holder with an EPTP MEMS device. The EPTP device contains a movable part and a fixed part, which are connected by springs; see Supporting Information S5. The electrical transport properties measurements were performed by sweeping the voltage applied on the nanowire from −0.5 to 0.5 V and measuring the current going through the nanowire. The electric current limit in the $I-V$ measurements was set to 100 nA to minimize the Joule heating effect. No changes in crystal structure and electrical transport properties of the nanowire due to the illumination of the electron beam in TEM were observed.

ASSOCIATED CONTENT

Supporting Information

The Supporting Information is available free of charge on the ACS Publications website at DOI: 10.1021/acs.nanolett.8b01782.

Estimation of the lattice mismatch between InAs and $In_{0.6}Ga_{0.4}As$, STEM images from different segments of the core-shell nanowire, SAED patterns, GPA analysis near the core-shell interface, EPTP device for in situ TEM measurements, sample preparation for in situ TEM, in situ TEM data acquisition prodedure, NBED pattern for strain measurement, $I-V$ measurements at different voltage ranges, repeated $I-V$ and strain measurements, comparison of strain measurements from NBED and nanoindenter displacement, electromechanical properties of a bare InAs nanowire measured with the EPTP device, and band-structure change as a function of tensile strain in InAs from tight-binding simulation (PDF)

AUTHOR INFORMATION

Corresponding Author

*E-mail: eva.olsson@chalmers.se.

ORCID

Lunjie Zeng: 0000-0002-4564-7217

Notes

The authors declare no competing financial interest.

ACKNOWLEDGMENTS

L.J.Z., W.J., and E.O. acknowledge the financial support from Swedish Research Council (VR) under grant no. 2016-04618, Nanoscience and Nanotechnology Area of Advance and Energy Area of Advance at Chalmers University of Technology. A.M. gratefully acknowledges funding from the U.S. Office of Naval Research under grant no. N00014-17-1-2283. Portions of this work were performed as a user project at the Molecular Foundry at Lawrence Berkeley National Laboratory, which is supported by the U.S. Department of Energy under contract no. DE-AC02-05CH11231. T.K. and P.K. acknowledge financial support by Microsoft Quantum and the European Research Council (ERC) under grant agreement no. 716655 (HEMs-DAM).

REFERENCES

(1) Dai, H.; Tombler, T. W.; Zhou, C.; Alexseyev, L.; Kong, J.; Liu, L.; Jayanthi, C. S.; Tang, M.; Wu, S.-Y. *Nature* **2000**, *405* (6788), 769−772.

(2) Wu, Z.; Neaton, J. B.; Grossman, J. C. *Nano Lett.* **2009**, *9* (6), 2418−2422.

(3) del Alamo, J. A. *Nature* **2011**, *479* (7373), 317−323.

(4) Ionescu, A. M.; Riel, H. *Nature* **2011**, *479* (7373), 329−337.

(5) Ko, H.; Takei, K.; Kapadia, R.; Chuang, S.; Fang, H.; Leu, P. W.; Ganapathi, K.; Plis, E.; Kim, H. S.; Chen, S.-Y.; Madsen, M.; Ford, A. C.; Chueh, Y.-L.; Krishna, S.; Salahuddin, S.; Javey, A. *Nature* **2010**, *468* (7321), 286−289.

(6) Wang, Z.; Tian, B.; Pantouvaki, M.; Guo, W.; Absil, P.; Van Campenhout, J.; Merckling, C.; Van Thourhout, D. *Nat. Photonics* **2015**, *9* (12), 837−842.

(7) Miao, J.; Hu, W.; Guo, N.; Lu, Z.; Zou, X.; Liao, L.; Shi, S.; Chen, P.; Fan, Z.; Ho, J. C.; Li, T. X.; Chen, X. S.; Lu, W. *ACS Nano* **2014**, *8* (4), 3628−3635.

(8) Krogstrup, P.; Jørgensen, H. I.; Heiss, M.; Demichel, O.; Holm, J. V.; Aagesen, M.; Nygard, J.; Fontcuberta i Morral, A. *Nat. Photonics* **2013**, *7* (4), 306−310.
(9) Chuang, S.; Gao, Q.; Kapadia, R.; Ford, A. C.; Guo, J.; Javey, A. *Nano Lett.* **2013**, *13* (2), 555−558.
(10) He, R.; Yang, P. *Nat. Nanotechnol.* **2006**, *1* (1), 42−46.
(11) Signorello, G.; Sant, S.; Bologna, N.; Schraff, M.; Drechsler, U.; Schmid, H.; Wirths, S.; Rossell, M. D.; Schenk, A.; Riel, H. *Nano Lett.* **2017**, *17* (5), 2816−2824.
(12) Lee, J. H.; Pin, M. W.; Choi, S. J.; Jo, M. H.; Shin, J. C.; Hong, S. G.; Lee, S. M.; Cho, B.; Ahn, S. J.; Song, N. W.; Yi, S. H.; Kim, Y. H. *Nano Lett.* **2016**, *16* (11), 6738−6745.
(13) Guilloy, K.; Pauc, N.; Gassenq, A.; Gentile, P.; Tardif, S.; Rieutord, F.; Calvo, V. *Nano Lett.* **2015**, *15* (4), 2429−2433.
(14) Ma, J. W.; Lee, W. J.; Bae, J. M.; Jeong, K. S.; Oh, S. H.; Kim, J. H.; Kim, S. H.; Seo, J. H.; Ahn, J. P.; Kim, H.; Cho, M. H. *Nano Lett.* **2015**, *15* (11), 7204−7210.
(15) Watanabe, K.; Nagata, T.; Wakayama, Y.; Sekiguchi, T.; Erdélyi, R.; Volk, J. *ACS Nano* **2015**, *9* (3), 2989−3001.
(16) Shao, R.; Zheng, K.; Wei, B.; Zhang, Y.; Li, Y.; Han, X.; Zhang, Z.; Zou, J. *Nanoscale* **2014**, *6* (9), 4936−4941.
(17) Signorello, G.; Lörtscher, E.; Khomyakov, P. A.; Karg, S.; Dheeraj, D. L.; Gotsmann, B.; Weman, H.; Riel, H. *Nat. Commun.* **2014**, *5*, 3655.
(18) Winkler, K.; Bertagnolli, E.; Lugstein, A. *Nano Lett.* **2015**, *15* (3), 1780−1785.
(19) Gooth, J.; Borg, M.; Schmid, H.; Schaller, V.; Wirths, S.; Moselund, K.; Luisier, M.; Karg, S.; Riel, H. *Nano Lett.* **2017**, *17* (4), 2596−2602.
(20) Zhou, X.; Dayeh, S. A.; Aplin, D.; Wang, D.; Yu, E. T. *Appl. Phys. Lett.* **2006**, *89* (5), 053113.
(21) Nadj-Perge, S.; Frolov, S. M.; Bakkers, E. P.; Kouwenhoven, L. P. *Nature* **2010**, *468* (7327), 1084−1087.
(22) Li, X.; Wei, X.; Xu, T.; Pan, D.; Zhao, J.; Chen, Q. *Adv. Mater.* **2015**, *27* (18), 2852−2858.
(23) Wang, F.; Yip, S.; Han, N.; Fok, K.; Lin, H.; Hou, J. J.; Dong, G.; Hung, T.; Chan, K. S.; Ho, J. C. *Nanotechnology* **2013**, *24* (37), 375202.
(24) Sun, M. H.; Joyce, H. J.; Gao, Q.; Tan, H. H.; Jagadish, C.; Ning, C. Z. *Nano Lett.* **2012**, *12* (7), 3378−3384.
(25) Du, J.; Liang, D.; Tang, H.; Gao, X. P. A. *Nano Lett.* **2009**, *9* (12), 4348−4351.
(26) van Tilburg, J. W. W.; Algra, R. E.; Immink, W. G. G.; Verheijen, M.; Bakkers, E. P. A. M.; Kouwenhoven, L. P. *Semicond. Sci. Technol.* **2010**, *25* (2), 024011.
(27) Jiang, X.; Xiong, Q.; Nam, S.; Qian, F.; Li, Y.; Lieber, C. M. *Nano Lett.* **2007**, *7* (10), 3214−3218.
(28) Ozdol, V. B.; Gammer, C.; Jin, X. G.; Ercius, P.; Ophus, C.; Ciston, J.; Minor, A. M. *Appl. Phys. Lett.* **2015**, *106* (25), 253107.
(29) Gammer, C.; Kacher, J.; Czarnik, C.; Warren, O. L.; Ciston, J.; Minor, A. M. *Appl. Phys. Lett.* **2016**, *109* (8), 081906.
(30) Ellaway, S. W.; Faux, D. A. *Phys. Status Solidi B* **2003**, *235* (2), 437−440.
(31) Thelander, C.; Caroff, P.; Plissard, S.; Dey, A. W.; Dick, K. A. *Nano Lett.* **2011**, *11* (6), 2424−2429.
(32) Chen, J. M.; MacDonald, N. C. *Rev. Sci. Instrum.* **2004**, *75* (1), 276−278.
(33) Tuzzolino, A. J. *Phys. Rev.* **1958**, *112* (1), 30.
(34) Woodall, J. M.; Freeouf, J. L.; Pettit, G. D.; Jackson, T.; Kirchner, P. *J. Vac. Sci. Technol.* **1981**, *19* (3), 626−627.
(35) Joyce, H. J.; Parkinson, P.; Jiang, N.; Docherty, C. J.; Gao, Q.; Tan, H. H.; Jagadish, C.; Herz, L. M.; Johnston, M. B. *Nano Lett.* **2014**, *14* (10), 5989−5994.
(36) Sun, Y.; Thompson, S. E.; Nishida, T. *Strain Effect in Semiconductors*; Springer US: Boston, MA, 2010.
(37) Sze, S. M.; Ng, K. K. *Physics of Semiconductor Devices*; Wiley-Interscience: Weinheim, Germany, 2007.
(38) Li, S.; Jiang, Q.; Yang, G. W. *Appl. Phys. Lett.* **2010**, *96* (21), 213101.
(39) Fu, Q.; Zhang, Z. Y.; Kou, L.; Wu, P.; Han, X.; Zhu, X.; Gao, J.; Xu, J.; Zhao, Q.; Guo, W.; Yu, D. *Nano Res.* **2011**, *4* (3), 308−314.
(40) Hong, K.-H.; Kim, J.; Lee, S.-H.; Shin, J. K. *Nano Lett.* **2008**, *8* (5), 1335−1340.
(41) Conzatti, F.; Pala, M. G.; Esseni, D.; Bano, E.; Selmi, L. *IEEE Trans. Electron Devices* **2012**, *59* (8), 2085−2092.
(42) Sun, Y.; Thompson, S. E.; Nishida, T. *J. Appl. Phys.* **2007**, *101* (10), 104503.
(43) Aspnes, D. E.; Cardona, M. *Phys. Rev. B: Condens. Matter Mater. Phys.* **1978**, *17* (2), 741−751.
(44) Hori, Y.; Ando, Y.; Miyamoto, Y.; Sugino, O. *Solid-State Electron.* **1999**, *43* (9), 1813−1816.
(45) Kisielowski, C.; Freitag, B.; Bischoff, M.; van Lin, H.; Lazar, S.; Knippels, G.; Tiemeijer, P.; van der Stam, M.; von Harrach, S.; Stekelenburg, M.; Haider, M.; Uhlemann, S.; Müller, H.; Hartel, P.; Kabius, B.; Miller, D.; Petrov, I.; Olson, E. A.; Donchev, T.; Kenik, E. A.; Lupini, A. R.; Bentley, J.; Pennycook, S. J.; Anderson, I. M.; Minor, A. M.; Schmid, A. K.; Duden, T.; Radmilovic, V.; Ramasse, Q. M.; Watanabe, M.; Erni, R.; Stach, E. A.; Denes, P.; Dahmen, U. *Microsc. Microanal.* **2008**, *14* (05), 469−477.
(46) Dahmen, U.; Erni, R.; Radmilovic, V.; Ksielowski, C.; Rossell, M.-D.; Denes, P. *Philos. Trans. R. Soc., A* **2009**, *367* (1903), 3795−3808.

DOI: 10.1021/acs.nanolett.8b01782
Nano Lett. 2018, 18, 4949−4956